Phase Demodulation Based on K-Space With High Sensitivity for Interferometric Fiber Sensor

Ling Chen, Jiewen Li, Jiajun Tian, Yang Bang, Kedi Tang, and Yong Yao

***Abstract*—This study firstly proposes and experimentally demonstrates a phase demodulation method with high sensitivity for interferometric fiber sensors (IFSs) on the basis of the fast Fourier transform of a wavenumber domain. The phase information of IFSs triggered by changes in environmental parameters is obtained by calculating the initial phase variation of a specific Fourier-transformed spatial frequency. Theoretically, phase sensitivity can be improved by *n* times when the optical path difference (OPD) of a spatial frequency peak is increased by a multiple (*n* times) of the OPD of other spatial frequency domain peaks. To verify the method experimentally, this study designed a large laterally offset spliced sensor formed by common single-mode fibers on the basis of mode interference. The sensing characteristics of temperature and strain in each set of two-beam interference are analyzed simultaneously by calculating the phase sensitivities of the frequency domain peaks. Furthermore, the highest reported temperature and strain sensitivities of 0.0795 rad/°C and −0.0088 rad/$\mu\varepsilon$, respectively, with good repeatability are realized.**

***Index Terms*—Fast Fourier transform, Interferometric fiber sensor, K-Space, Optical path difference, Phase demodulation.**

I. Introduction

INTERFEROMETRIC fiber sensors (IFSs) are widely used for measuring external environmental parameters, including gas refractive indices [1], temperature [2], [3], [4], strain [5], [6], salinity [7], glucose [8], force [9] and respiration [10], because of their many advantages, such as low cost, simple fabrication, small size, anti-electromagnetic interference and high sensitivity/resolution. Generally, IFSs can simultaneously measure dual parameters [11], [12]. More importantly, the dual-parameter simultaneous measurement of temperature and strain occupies a key position in structural health and environmental monitoring [13]. The wavelength-tracking demodulation (WTD) method is typically used in environmental parameter measurements (via an optical spectrum analyzer [OSA]) to track the dip (peak) wavelength shift of IFSs caused by variations in physical parameters. However, spectral noise and wavelength sampling rates may cause unpredictable errors, which could affect the accuracy of experimental results [14]. Additionally, OSAs have resolution limits, which unavoidably impacts the resolution of optical sensors.

Compared with the traditional WTD method, phase demodulation technology is extremely effective in preventing errors caused by spectral noise and sampling intervals, which is beneficial for ensuring the accuracy of experimental results. This compensates for the shortcomings of the lower-accuracy WTD method.

First, spatial frequency spectra (SFS) containing one or several frequency peaks corresponding to one or several sets of two-beam interference (TBI) are obtained via fast Fourier transform (FFT) from interference optical spectra in the wavelength domain (WLD) (λ-space) [15], [16], [17], [18]. Phase demodulation is realized by calculating the variation in the initial phase of each spatial frequency peak caused by variations in external environmental parameters. Recently, the IFS-based phase demodulation method has been reported to offer good performance advantages. For example, Fu *et al.* proposed a multimode interferometer on the basis of an offset spliced single-mode fiber (SMF) structure with temperature and strain sensitivities of only −0.026 rad/°C and 0.0003 rad/$\mu\varepsilon$, respectively [14]. Nan *et al.* used a suspended-core microstructure optical fiber sensor for temperature measurement with a low sensitivity of −0.011 rad/°C on the basis of phase demodulation [19]. Galarza *et al.* proposed a new liquid-level sensor multiplexed system on the basis of multimode interference microfibers with a sensitivity of 11.4 rad/mm [20].

However, the phase modulation method has not been fully developed. For example, how to effectively improve the phase sensitivity of IFSs remains problematic. Additionally, The SFS of λ-space is particularly messy, and it is difficult to analyze specific interference components (especially multibeam interference coexisting in one IFS) when Fourier transform is conducted directly on WLDs. Therefore, to solve these problems, SFS based on wavenumber domain (WND) (k-space) are firstly obtained via FFT operation on k-space converted from WLD by linear-in-wavenumber resampling, which is extremely effective for separating every frequency peak and avoiding spectral artifact peaks [21], [22].

This study proposes a temperature and strain large-offset spliced SMF IFS with high sensitivity on the basis of phase modulation by calculating the sensor's phase variation in the

Manuscript received 21 April 2022; revised 21 June 2022; accepted 23 June 2022. Date of publication 28 June 2022; date of current version 11 July 2022. This work was supported in part by Shenzhen Science and Technology Program Project under Grants JCYJ20190806143818818 and GXWD20201230155427003-20200731103843002, and in part by the National Natural Science Foundation of China under Grant 61675055. *(Ling Chen and Jiewen Li contributed equally to this work.) (Corresponding author: Jiajun Tian.)*

The authors are with the Department of Electronic and Information Engineering, Harbin Institute of Technology, Shenzhen, Guangdong Province 518055, China (e-mail: 21b952004@stu.hit.edu.cn; 20b952013@stu.hit.edu.cn; tianjiajun@hit.edu.cn; 1572862975@qq.com; 190210425@stu.hit.edu.cn; yaoyong@hit.edu.cn).

Digital Object Identifier 10.1109/JPHOT.2022.3186737

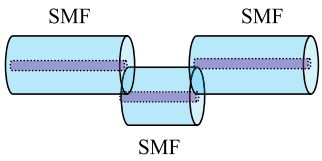

Fig. 1. Schematic diagram of single-mode fiber large-offset spliced fiber optic sensor.

Fourier domain. The phase variation can be obtained by analyzing the intrinsic spatial frequency peaks in k-space, which contain the most energy in a fiber interferometer. According to theoretical derivation and experimental validation, if the OPD of one frequency peak is *n* times that of other spatial frequency peaks, the corresponding phase sensitivity will have an identical relationship. In this study, the temperature and strain sensitivities are 3 and 29 times higher, respectively, than those reported for the same type of IFS; these values are the highest reported for IFS structures based on phase modulation.

II. Principle and Numerical Analysis

The energy in an IFS is mainly distributed on several main spatial frequency domain peaks and contains the phase information of the optical fiber sensor. To better understand the principle of phase modulation method, a compact large intentional lateral offset in-fiber interferometer was fabricated by splicing a short section of SMF between two SMF sections, as shown in the schematic diagram in Fig. 1. Substantial misalignments in higher-order cladding modes cause excitation. Because of the large refractive index difference between the air cavity and cladding of SMFs, different OPDs can be obtained by adjusting the lengths of the SMFs sandwiched between two SMF sections [23], [24].

The expression of TBI model-based SMF large-offset fiber interferometer is constructed as (1) according to [25]. The terms I_1 and I_2 represent the intensities of two lights; d and φ are the OPD and phase difference, respectively; and A and B are two constants related to the optical intensity and coupling ratio between two optical paths.

$$\mathrm{I}(\lambda) = \mathrm{I}_1 + \mathrm{I}_2 + 2\sqrt{\mathrm{I}_1\mathrm{I}_2}\cos\frac{2\pi}{\lambda}\cdot d = A + B\cos\frac{2\pi}{\lambda}\cdot d \quad (1)$$

$$\varphi = \frac{2\pi}{\lambda}\cdot d \quad (2)$$

There will be a monotonic spectral shift along with the variation in the OPD of the IFS caused by the environmental parameters expressed in (3), in which Δd and $\Delta\lambda$ are the OPD variation and wavelength shift value, respectively:

$$\mathrm{I}'(\lambda) = A + B\cos\frac{2\pi}{\lambda}\cdot(d-\Delta d) = \mathrm{I}(\lambda+\Delta\lambda) \quad (3)$$

However, several multibeam interferences usually coexist in an IFS. When the wavelength range (span) is large, the direct Fourier transform on the WLD often results in the expansion and overlap of spatial frequency lines, which makes it difficult to analyze the interference components correctly [26]. To solve this problem, λ-space is firstly converted into k-space on the basis of linear-in-wavenumber resampling to eliminate the influence caused by nonlinearity between the phase difference and wavelength. Therefore, Eq. (1) can be rewritten as (4) and the phase difference (φ) is a linear relationship with wavenumber *k* defined as (5). The terms k_j, λ_i and Δk_j denote the wavenumber sample, wavelength sample and error caused by resampling in (5), respectively. Wavelength sample (λ_i) is sampled at equal intervals of wavelength which is replaced by wavenumber at the same number of samples k_j with equal intervals. Therefore, there is a little error at each point. However, since the phase demodulation method is operated based on the overall Fourier transform, Δk_j has little influence on the obtained phase information. The principle of linear-in-wavenumber resampling is illustrated in Fig. 2(a).

$$\mathrm{I}(k_j) = \mathrm{I}_1 + \mathrm{I}_2 + 2\sqrt{\mathrm{I}_1\mathrm{I}_2}\cos[(k_j - \Delta k_j)\cdot d](j = 1,2,3\ldots\ldots) \quad (4)$$

$$k_j - \Delta k_j = \frac{2\pi}{\lambda_i}\ (i = 1,2,3\ldots\ldots) \quad (5)$$

Using the example of TBI, Fig. 2(b) and (c) show the simulated interference spectra of the different wavelength spans (100 nm, 150 nm, 200 nm) and corresponding wavenumber domains (0.208 × 10^{-3} rad/nm, 0.406 × 10^{-3} rad/nm, 0.525 × 10^{-3} rad/nm), where the values of I_1, I_2 and d are set as 1 mW, 1 mW and 268 μm, respectively. The SFS of the Fourier transforms on λ-space and k-space with wavelength spans of 50 (1600–1650), 200 (1450–1650), 300 (1350–1650) and 400 nm (1250–1650 nm), respectively are presented in Fig. 2(d) and (e). A comparison of Fig. 2(d) and (e) reveals that, when the wavelength span is small, the SFS on the λ-space and k-space are basically the same. As the spans increase, the SFS on the k-space can be distinguished clearly and ensure the accuracy of phase modulation, although those on the λ-space are widened. The greater the span, the more serious the SFS expansion phenomenon. The spatial frequency distribution is obtained by performing FFT operation on (4):

$$F(f_m) = \mathrm{F}\ (\mathrm{I}(k_j)) = \sum_{j=1}^{\mathrm{N}}[\mathrm{I}_1+\mathrm{I}_2]\ \cos[(k_j-\Delta k_j)\cdot d]\,\mathrm{e}^{-j2\pi f_m k_j} \quad (6)$$

$$\varphi\ (f_m) = \arctan\left\{\frac{\mathrm{I}_m[\mathrm{F}(f_m)]}{R_e[\mathrm{F}(f_m)]}\right\} \quad (7)$$

$$\varphi'\ (f_m) = \arctan\left\{\frac{\mathrm{I}_m[\mathrm{F}'(f_m)]}{\mathrm{R}_e[\mathrm{F}'(f_m)]}\right\} \quad (8)$$

Where $\mathrm{I}_m[\mathrm{F}(f_m)]$ and $R_e[\mathrm{F}(f_m)]$ are the imaginary and real parts, respectively of the FFT results at the intrinsic spatial frequency $f_m \cdot \mathrm{F}'(f_m)$ is the spatial frequency distribution of $\mathrm{I}'(k_j)$. Then, the variation in the initial phase $\Delta\varphi$ can be

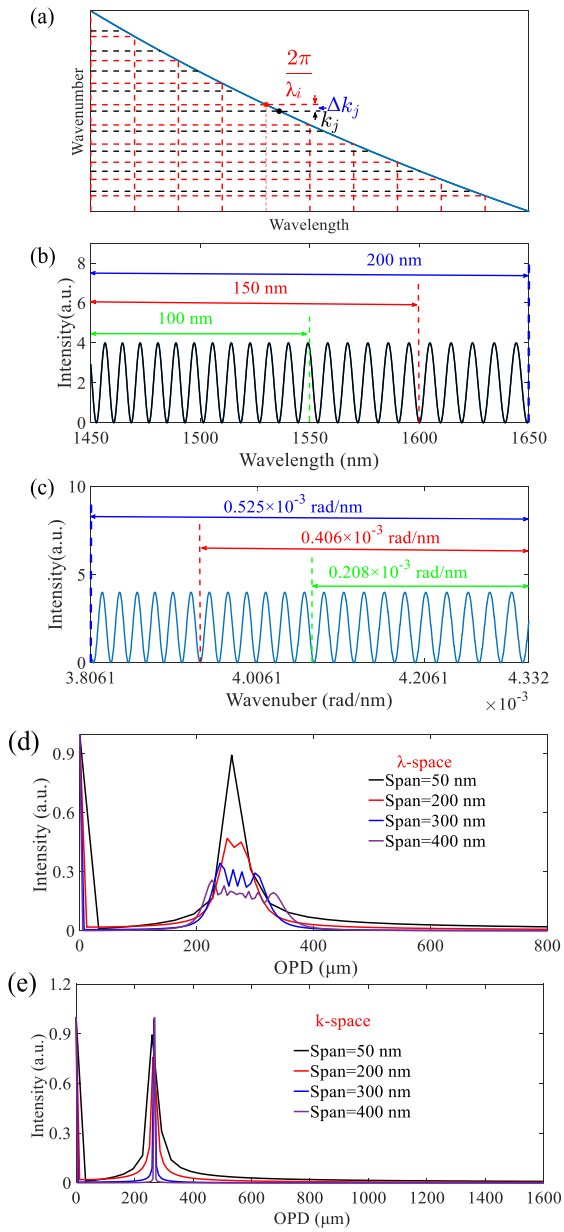

Fig. 2. Simulated results: (a) The principle of linear-in-wavenumber resampling; (b) Simulated TBI spectrum of different wavelength spans; (c) Simulated TBI spectrum based on linear-in-wavenumber resampling in (a); (d) Spatial frequency spectra (SFS) of TBI with different spans (50, 200, 300 and 400 nm) based on λ-space; (e) SFS of TBI with different spans (50, 200, 300 and 400 nm) based on k-space.

calculated using (9):

$$\begin{aligned}\Delta\varphi &= \varphi'(f_m) - \varphi(f_m)\\ &= \arctan\left\{\frac{\mathrm{I}_m[\mathrm{F}'(f_m)]}{R_e[\mathrm{F}'(f_m)]}\right\}\\ &\quad - \arctan\left\{\frac{\mathrm{I}_m[\mathrm{F}(f_m)]}{R_e[\mathrm{F}(f_m)]}\right\}\\ &= \arctan\left\{\frac{\frac{\mathrm{I}_m[\mathrm{F}'(f_m)]}{R_e[\mathrm{F}'(f_m)]} - \frac{\mathrm{I}_m[\mathrm{F}(f_m)]}{R_e[\mathrm{F}(f_m)]}}{1+\frac{\mathrm{I}_m\mathrm{F}'(f_m)\mathrm{I}_m[\mathrm{F}(f_m)]}{R_e[\mathrm{F}'(f_m)]R_e[\mathrm{F}(f_m)]}}\right\}\end{aligned} \tag{9}$$

When environmental parameters cause the OPD to change, Eq. (4) can be further rewritten as (10). The term k_j is a constant that represents phase sensitivity. The wavenumber shift is denoted as δk_j, which can be regarded as a constant because the value of Δd is too small compared with d.

$$\begin{aligned}\mathrm{I}'(k_j) &= \mathrm{I}_1 + \mathrm{I}_2 + 2\sqrt{\mathrm{I}_1\mathrm{I}_2}\cos[(k_j - \Delta k_j)\cdot(d-\Delta d)]\\ &\approx \mathrm{I}_1 + \mathrm{I}_2 + 2\sqrt{\mathrm{I}_1\mathrm{I}_2}\cos[(k_j + \delta k_j\Delta k_j)\cdot d]\\ &= \mathrm{I}_1 + \mathrm{I}_2 + 2\sqrt{\mathrm{I}_1\mathrm{I}_2}\cos[(k_j - \Delta k_j)\cdot d + \delta\varphi_j]\\ &= (k_j + \delta\varphi_j)\end{aligned} \tag{10}$$

$$\delta k_j = \frac{k_j\cdot\Delta d}{d} \tag{11}$$

$$\delta\varphi_j = \delta\varphi_j\cdot d = k_j\cdot\Delta d \tag{12}$$

$$n\delta\varphi_j = \delta k_j\cdot nd \tag{13}$$

According to (11) and (12), the variation in the initial phase of a specific spatial frequency ($\delta\varphi_j$) is linear with d and Δd. If the OPDs of different frequency peaks have multiple relationship, the corresponding phase sensitivities will also have the same multiple relationship, as summarized in (13). Therefore, theoretically, the phase sensitivity of the IFS can be increased by *n* times based on this principle. Taking the SMF large-offset fiber structure as a multimode interference model, this study constructed a theoretical simulation on the basis of three-beam interference to further confirm the feasibility of the proposed phase sensitivity improvement method, which is expressed as (14). The length of the sandwiched SMF is assumed to be 750 μm, and the refractive indices of the core, cladding and air are 1.453, 1.444 and 1, respectively. The OPDs between the different modes are determined to be approximately 268, 283 and 551 μm. There is small difference between the OPD of peak 1 ($d_1 = 268$ μm) and peak 2 ($d_2 = 283$ μm). The sum of $d_1$and d_2 is equal to the OPD of peak 3 ($d_3 = 551$ μm), which is about double that of d_1 and d_2, according to (13).

$$\begin{aligned}\mathrm{I}(\lambda) &= \mathrm{I}_1 + \mathrm{I}_2 + \mathrm{I}_3 + 2\sqrt{\mathrm{I}_1\mathrm{I}_2}\cos\frac{2\pi}{\lambda}\cdot d_1\\ &\quad + 2\sqrt{\mathrm{I}_2\mathrm{I}_3}\cos\frac{2\pi}{\lambda}\cdot d_2\\ &\quad + 2\sqrt{\mathrm{I}_1\mathrm{I}_3}\cos\frac{2\pi}{\lambda}\cdot d_3\end{aligned} \tag{14}$$

The interference spectrum has a constant wavelength shift caused by external environmental parameters and its spectral shape remains constant [14]. Fig. 3(a) and (b) present the simulated interference spectra based on WLD and WND without waveform disturbance, where I_1, I_2, I_3, d_1, d_2 and d_3 are 2, 0.1 and 0.1 mW and 268, 283 and 551 μm, respectively. The OPD increases in 0.1 μm increments. As shown in Fig. 3(c), the corresponding SFS are obtained via FFT on k-space (black line) and λ-space (red line). The specific interference components cannot be distinguished from the SFS of λ-space, and they even cause mistakes when analyzing the interference components. However, SFS of k-space clearly reflects three-beam interference, which, essentially, is the same as the OPD value set by the numerical simulation. The simulated phase sensitivity is presented in Fig. 3(d) whose relationship conforms to (13).

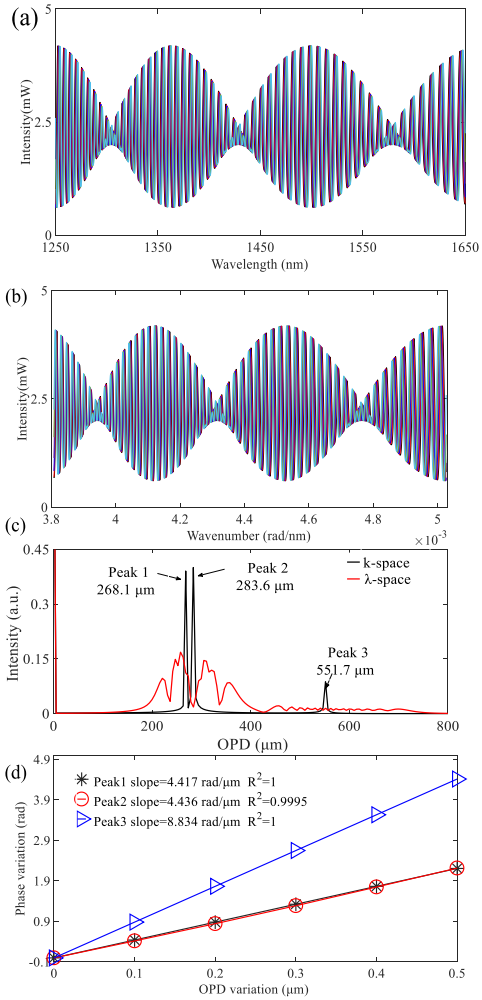

Fig. 3. Simulated results: (a) Simulated three-beam interference spectrum when the OPD increases in 0.1 μm increments; (b) Simulated three-beam interference spectrum based on linear-in-wavenumber resampling in (a) when the OPD increases in increments of 0.1 μm; (c) SFS of three-beam interference based on k-space (black line) and λ-space (red line); (d) The relationship of three spatial frequency peaks between OPD variation and phase variation.

Accordingly, it can be concluded that peaks 1 and 2 have the same phase sensitivity value, i.e., half that of peak 3. To further enhance the phase sensitivity, this study extended three-beam interference to six-beam interference, which was simulated with OPD variations of 0.01 μm (see Fig. 4(a)–(d) for the interference spectra and corresponding SFS). Additionally, the result in Fig. 4(d) demonstrates the simulated phase sensitivities of peaks 7 (1067), 6 (804.4) and 5 (536.3 μm) is 4, 3 and 2 times of peak 4 (268.1 μm), respectively. In short, the proposed method has groundbreaking significance in terms of enhancing phase sensitivity.

The accuracy of phase demodulation is affected by the OPD variation step which depends on the change of the external environment parameters. The OPD variation steps of 10^{-14}, 10^{-13} and 10^{-12} μm were selected for analyzing with numerical simulation where initial OPD, wavelength interval and wavelength span were 250 μm, 001 nm and 400 nm (1250 nm–1650 nm) respectively. The accuracies of phase modulation for different

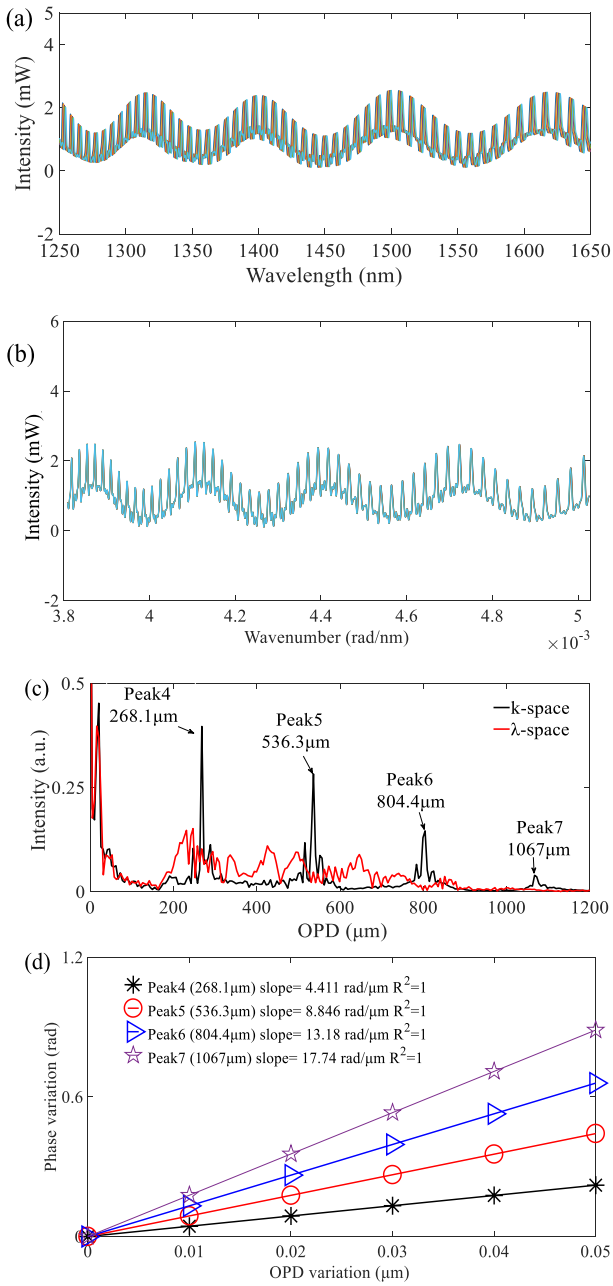

Fig. 4. (a) Simulated six-beam interference spectrum when the OPD increases in increments of 0.01 μm; (b) Simulated six-beam interference spectrum based on linear-in-wavenumber resampling in (a) when the OPD increases in increments of 0.01 μm; (c) SFS of six-beam interference based on k-space (black line) and λ-space (red line); (d) The relationship of four main frequency peaks between OPD variation and phase variation.

OPD variation steps (10^{-14}, 10^{-13} and 10^{-12} μm) were presented in Fig. 5(a)–(c), respectively. When the OPD variation steps is 10^{-13} and 10^{-12} μm, high phase modulation accuracies were obtained with excellent linear correlation coefficient of 0.9954 and 0.9999. However, when the OPD variation step is 10^{-14} μm, the accuracy of phase modulation is low and the linear correlation coefficient is only 0.9299.

Finally, the sensing range of phase modulation was analyzed and discussed. The measurement range is limited because of the

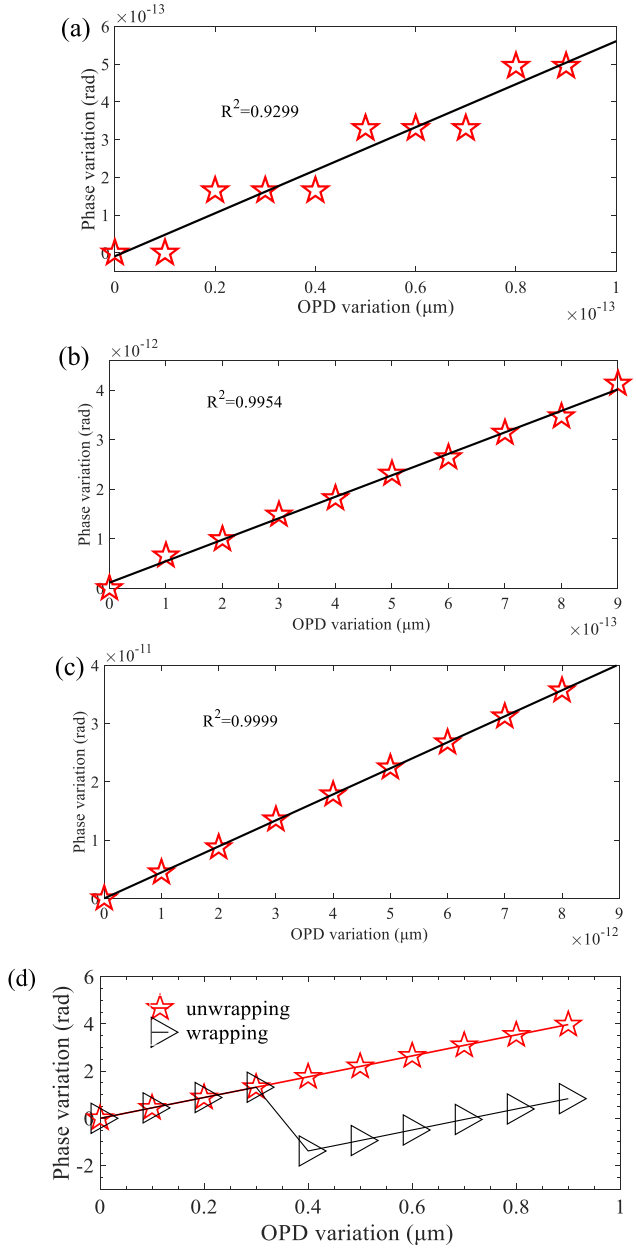

Fig. 5. The accuracies of phase demodulation for different OPD variation steps: (a) 10^{-14} μm; (b) $10^{-13}\mu$m; (c) 10^{-12} μm; (d) the comparison of phase unwrapping and wrapping.

arctangent function with angular range restriction $(-\pi/2, \pi/2)$. In order to solve this problem, the initial phase is expanded to realize the phase unwrapping shown in Fig. 5(d). The measurement range of phase modulation can be further improved after phase unwrapping.

III. Experimental Results and Discussion

The phase modulation method with general applicability and great performance advantages can be applied for IFSs including reflection and transmission type. Each frequency domain peak of SFS based on k-space is perfectly separated and there is a one-to-one correspondence between the frequency domain peak

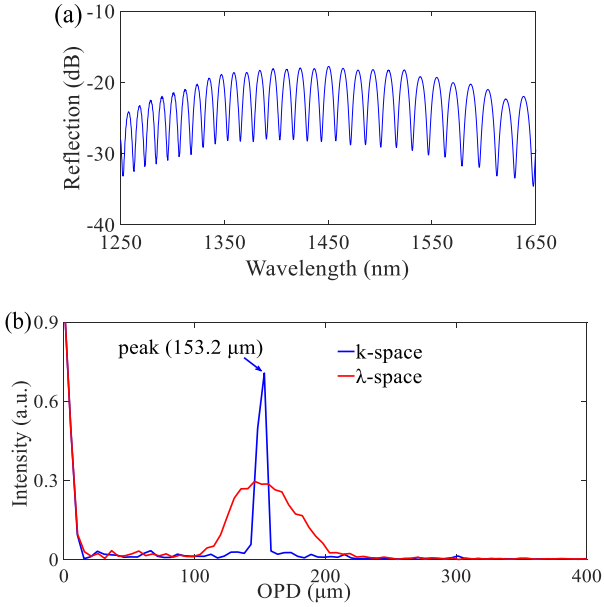

Fig. 6. Measured results of FPI: (a) The reflection spectrum of FP sensor; (b) the SFS based on k-space (black line) and λ-space (red line).

and OPD. In addition, it is also a powerful tool to accurately reflect the cavity length for FPI sensor. Therefore, there is no need to calibrate the cavity length by special software. In order to verify the practicability and feasibility of the phase modulation method, optical fiber sensors based on reflection and transmission type were fabricated for experimental verification.

A. Reflection Type

A cavity length of 76 μm SMF (Corning, ITU-T G.652.D) with offset of 80 μm was sandwiched between two sections of SMFs to form the Fabry-Perot interferometer (FPI) with two reflected mirrors composed of interfaces between the fiber end face and the air ($n_{\text{air}} = 1$). To ensure the accuracy of the cleaved length, cleaving was conducted under a microscope. The three ports of the optical circulator were connected to the broadband light source (BBS) (FiberLake ASE), OSA (AQ6370C) and FP sensor respectively. The light emitted from the BBS is reflected at the two reflected mirrors with reflectivity of 4%. The reflection spectrum in air and corresponding SFS based on k-space (black line) and λ-space (red line) were shown in Fig. 6(a)–(b), respectively. The calculated OPD (152 μm) between the two reflected beams of FP sensor is twice the cavity length (76 μm) which perfectly matches the OPD (153.2 μm) obtained by FFT operation in WND. Therefore, there is one-to-one correspondence between the peak and the OPD component. It lays the foundation for the subsequent dual-parameter simultaneous measurement.

B. Transmission Type

The performance of the proposed scheme was evaluated via a series of temperature and strain experiments. An IFS structure with a large 78 μm offset was simply formed by fusion; a 746

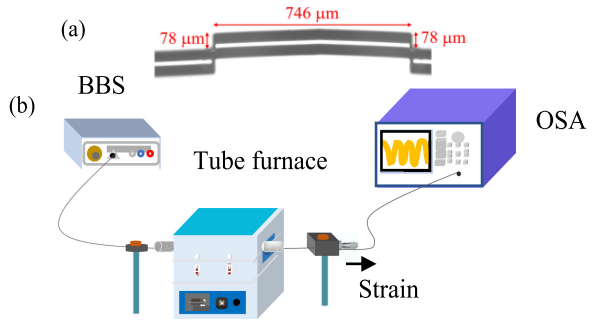

Fig. 7. (a) Microscopy image of fabricated single-mode fiber large-offset optical fiber sensor; (b) Schematic diagram of experimental device for simultaneous measurement of temperature and strain.

μm length of SMF was spliced between two sections of SMFs (see the microscopic image in Fig. 7(a)).

At the first splice point, a mismatch in the field modes caused the excitation of the higher cladding modes. The optical signal emitted from a BBS was recoupled at the second splice point received by the OSA. To ensure that the temperature was accurately controlled, the fabricated sensor was placed in a high-temperature tube furnace (SG-XL 1200, SIOM). As the external temperature changes, the refractive index and length of the IFS will also change because of thermo-optic and thermal expansion effects.

The interference spectrum exhibited a red shift when the temperature increased from 30 °C to 80 °C in 10 °C steps. Fig. 8(a) and (b) show the interference spectra based on λ-space and k-space, which is in good agreement with the simulation results. The corresponding SFS based on k-space and λ-space is presented in Fig. 8(c) and (d) formed by three beams and each peak corresponds to one TBI with OPD values of 268.1 (peak 1), 283.6 (peak 2) and 551.7 μm (peak 3), respectively. This indicates the excited two cladding modes interfere with the light propagating through the air. The temperature experiments involving heating and cooling processes were repeated for three times and experimental results indicated the sensor had good repeatability with a small error bar.

As can be seen in Fig. 8(d) and (e), the average temperature sensitivities of peaks 1, 2 and 3 were 0.0185, 0.0215 and 0.0384 rad/°C, respectively, in the heating process and 0.0189, 0.0209 and 0.0402 rad/°C, respectively, in the cooling process. Then, the sensor was fixed on two precision transmission platforms with an initial distance of 20 cm in the strain-sensing experiment. The interference spectrum showed a monotonous blue shift when the strain gradually increased from 0 to 600 $\mu\varepsilon$ in increments of 100 $\mu\varepsilon$. As shown in Fig. 8(f), the strain sensitivities of peaks 1, 2 and 3 were −0.0028, −0.00281 and −0.00476 rad/$\mu\varepsilon$, respectively, with high linear correlation coefficients of 0.9987, 0.9986 and 0.9984, respectively. Since the difference in OPD between peaks 1 and 2 is small (15 μm) and the sum of the two is equal to the OPD of peak 3. Essentially, the temperature and strain sensitivities of peaks 1 and 2 are basically the same. The temperature and strain sensitivities of peak 3 are approximately twice those

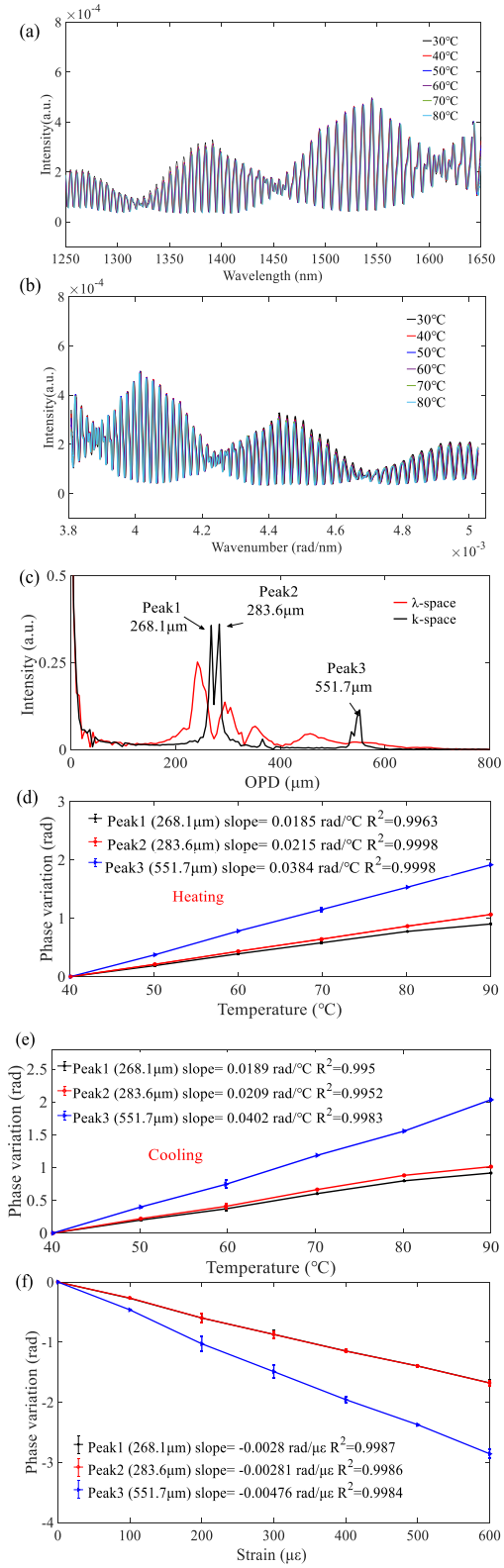

Fig. 8. Measured results: (a) Spectral response of the fabricated sensor with a sandwiched single-mode fiber length of 746 μm vs. temperature variations from 30 °C to 80 °C; (b) Interference spectrum based on linear-in-wavenumber resampling in (a); (c) Spatial frequency spectra based on λ-space and k-space; (d) The phase variation of the sensor when temperature increased from 30 °C to 80 °C for three times; (e) Phase variation of the optical fiber sensor when the temperature varied from 80 °C to 30 °C for three times. (f) Phase variation of the fabricated sensor when strain increased from 0 to 600 $\mu\varepsilon$ for three times.

of peaks 1 and 2. The temperature and strain sensitivities based on phase demodulation are consistent with theoretical derivation according to (13).

When the OPDs of different interference components have multiple relationship, the phase sensitivity can be further improved by exciting more multibeam interferences. For verification, the length of the sandwiched SMF was increased to 1210 μm to excite additional cladding modes.

Fig. 9(a)–(c) show the interference spectra of the SMF large-offset IFS based on λ-space and k-space and corresponding SFS. Multibeam interference was obtained where the OPDs of peaks 5 (536.3), 6 (804.4) and 7 (1067 μm) were 2, 3 and 4 times that of peak 4 (268.1 μm). The average temperature and strain sensitivities corresponding to peaks 4, 5, 6 and 7 were 0.0216, 0.0406, 0.0591, and 0.0795 rad/°C and −0.0023, −0.0047, −0.0063 and −0.0088 rad/$\mu\varepsilon$, respectively, as presented in Fig. 9(d) and (e). The temperature and strain sensitivities of peaks 7, 6 and 5 were 4, 3 and 2 times those of peak 4, respectively. The temperature and strain sensitivities of the IFS based on phase modulation methods are the highest among the all-fiber structures reported to date. The temperature and strain sensitivities based on phase modulation are 3 and 29 times higher than those of the same type of optical fiber sensor reported in the published literature [14].

The relationship between the improved sensitivities and the phase demodulation method is discussed in detail. According to (13), the phase sensitivities corresponding to different frequency domain peaks (OPDs with multiple relationship) have the same multiple relationship as the temperature and strain change. The larger the OPD, the larger the corresponding total initial phase variations. Compared with peak 4, The OPD of peak7 is larger which actually corresponds to a larger sensing length based on theoretical analysis. Therefore, the accumulated initial phase variations are more than peak 4 (reflected in improved sensitivity) under the same external disturbance. The other OPDs (peak7, peak6, peak5) and first OPD (peak4) of fabricated sensor satisfy multiple relationship (4 times, 3 times, 2 times). Experimental results show the temperature and strain sensitivities of peak7 (0.0795 rad/°C, −0.0088 rad/$\mu\varepsilon$) based on phase demodulation are about four times of peak4 (0.0216 rad/°C, −0.0023 rad/$\mu\varepsilon$). Thence, experimental results perfectly match with theoretical analysis. In theory, when other OPD is n times of the first OPD, the phase sensitivity can be improved n times.

The different interference peaks have different sensing responses as external temperature and strain changes. Therefore, simultaneous measurement can be achieved using a sensitivity matrix, which can be calculated using (15) and (16) [27], [28], [29]. Here, φ_{peak6} and φ_{peak7} represent the phase variations caused by changes in temperature (δT) and strain (δS). A schematic diagram showing the experimental device for the simultaneous measurement of temperature and strain can be seen in Fig. 7(b). Peaks 6 and 7 were selected for dual-parameter simultaneous measurement because of their higher phase sensitivity. When the solvable condition $C \neq 0$ is satisfied, (16) has

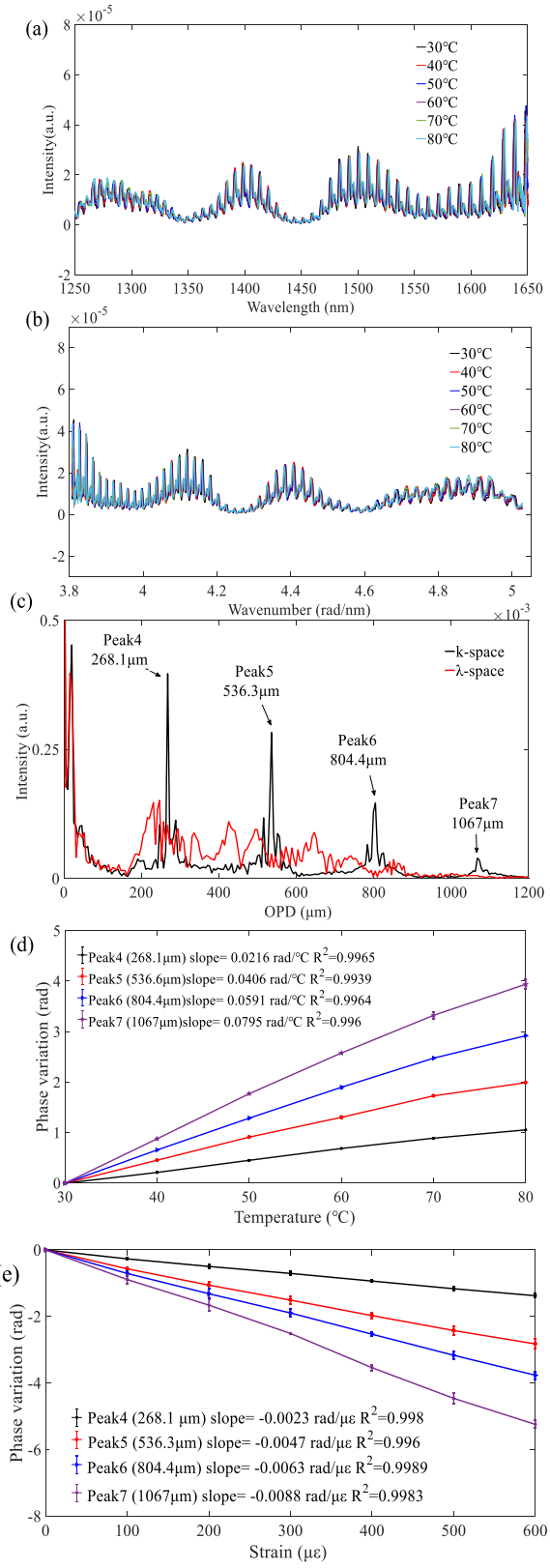

Fig. 9. Measured results: (a) Spectral response of the fabricated sensor with offset length of 1210 μm; (b) Spectral response based on linear-in-wavenumber resampling in (a); (c) Spatial frequency spectra based on λ-space and k-space; (d) Phase variation of the sensor when temperature increased from 30 °C to 80 °C for three times; (e) Phase variation of the sensor when strain increased from 0 to 600 $\mu\varepsilon$ for three times.

TABLE I
COMPARISON OF PERFORMANCE OF DIFFERENT SENSOR STRUCTURES FOR PHASE DEMODULATION

Sensor structure	Temperature sensitivity (rad/°C)	Strain sensitivity (rad/με)	References
SMF offset spliced	−0.026	0.0003	[14] (2017)
suspended-core microstructure optical fiber	−0.011	NA	[19] (2020)
Si inlay	0.063	NA	[30] (2021)
Fabry–Perot interferometers	NA	0.0034	[31] (2019)
SMF large-offset splicing	0.0795	−0.0088	**Proposed in this study**

a unique solution, which means that the simultaneous measurement of temperature and strain is feasible.

$$\begin{bmatrix}\delta\varphi_{\mathrm{peak6}}\\ \delta\varphi_{\mathrm{peak7}}\end{bmatrix}=\begin{bmatrix}S_{\mathrm{peak6,T}} & S_{\mathrm{peak6,S}}\\ S_{\mathrm{peak7,T}} & S_{\mathrm{peak7,S}}\end{bmatrix}\begin{bmatrix}\delta T\\ \delta S\end{bmatrix} \tag{15}$$

$$\begin{bmatrix}\delta T\\ \delta S\end{bmatrix}=\begin{bmatrix}0.0591\,\mathrm{rad}/^{\circ}\mathrm{C} & -0.0063\,\mathrm{rad}/\mu\varepsilon\\ 0.0795\,\mathrm{rad}/^{\circ}\mathrm{C} & -0.0088\,\mathrm{rad}/\mu\varepsilon\end{bmatrix}^{-1}\begin{bmatrix}\delta\varphi_{\mathrm{peak6}}\\ \delta\varphi_{\mathrm{peak7}}\end{bmatrix} \tag{16}$$

$$C=S_{\mathrm{peak6,T}}\,S_{\mathrm{peak7,S}}-S_{\mathrm{peak6,S}}S_{\mathrm{peak7,T}}\neq 0 \tag{17}$$

Table I compares the performance of different sensors based on phase demodulation. It can be seen that the method proposed in this study has outstanding performance advantages in terms of phase sensitivity improvement. The temperature and strain sensitivities of the SMF large-offset spliced sensor structure based on phase demodulation are the highest reported to date.

VI. CONCLUSION

In conclusion, this study theoretically proposed and experimentally demonstrated a high-sensitivity SMF large-offset IFS on the basis of phase demodulation technology in WND. The experimental results agree well with the theoretical simulation. The temperature and strain sensitivities of the fabricated sensor reached 0.0795 rad/°C and -0.0088 rad/$\mu\varepsilon$, which are the highest among the phase modulation-based all-in fiber IFSs reported to date. Temperature and strain were measured simultaneously by tracing the Fourier phase variation of different spatial frequency domain peaks of k-space. Theoretically, a phase sensitivity increase of *n* times can be achieved when the OPD of the frequency domain peak is *n* times that of other frequency domain peaks. Therefore, the proposed scheme has a controlling effect on the enhancement of phase sensitivity in optical fiber sensors.

REFERENCES

[1] D. W. Duan, Y. J. Rao, L. C. Xu, T. Zhu, D. Wu, and J. Yao, "In-fiber Mach-Zehnder interferometer formed by large lateral offset fusion splicing for gases refractive index measurement with high sensitivity," *Sensors Actuators, B: Chem.*, vol. 160, no. 1, pp. 1198–1202, 2011.

[2] J. Liu *et al.*, "Mach-Zehnder interferometer for high temperature (1000 °C) sensing based on a few-mode fiber," *Photonic Sensors*, vol. 11, no. 3, pp. 341–349, 2021.

[3] H. Chen *et al.*, "In-line interferometric temperature sensor based on dual-core fiber," *IEEE Sensors J.*, vol. 21, no. 10, pp. 12 146–12 152, May 2021.

[4] J. A. Flores-Bravo, M. A. Illarramendi, J. Zubia, and J. Villatoro, "Optical fiber interferometer for temperature-independent refractive index measuring over a broad range," *Opt. Laser Technol.*, vol. 139, 2021, Art. no. 106977.

[5] H. Zhang, M. Zhang, J. Kang, X. Zhang, and J. Yang, "High sensitivity fiber-optic strain sensor based on modified microfiber-assisted open-cavity Mach-Zehnder interferometer," *J. Lighw. Technol.*, vol. 39, no. 13, pp. 4556–4563, Jul. 2021.

[6] S. Wang *et al.*, "Ultrasensitive strain sensor based on Mach-Zehnder interferometer with bent structures," *J. Lightw. Technol.*, vol. 39, no. 21, pp. 6958–6967, Nov. 2021.

[7] N. Xie, H. Zhang, B. Liu, H. Liu, T. Liu, and C. Wang, "In-line microfiber-assisted Mach-Zehnder interferometer for microfluidic highly sensitive measurement of salinity," *IEEE Sensors J.*, vol. 18, no. 21, pp. 8767–8772, Nov. 2018.

[8] N. Xie, H. Zhang, B. Liu, J. Wu, and B. Song, "Highly sensitive in-line micro fluidic sensor based on micro fiber-assisted Mach–Zehnder interferometer for glucose sensing," *J Opt.*, vol. 19, no. 11, 2017, Art. no. 115803.

[9] Y. Wu *et al.*, "Highly sensitive force sensor based on balloon-like interferometer," *Opt. Laser Technol.*, vol. 103, pp. 17–21, 2018.

[10] Y. L. Wang *et al.*, "Low-cost wearable sensor based on a D-shaped plastic optical fiber for respiration monitoring," *IEEE Trans. Instrum. Meas.*, vol. 70, 2021, Art. no. 4004808.

[11] J. Li, Q. He, Z. Chen, and X. Fang, "Simultaneous measurement of three parameters based on an up-tapered fiber cascaded with a droplet-like multimode interferometer," *OSA Continuum*, vol. 2, no. 4, 2019, Art. no. 1113.

[12] Y. Wu, Y. Zhang, J. Wu, and P. Yuan, "Simultaneous measurement of transverse load and temperature using hybrid structured fiber-optic Fabry-Perot interferometer," *Sci. Rep.*, vol. 7, no. 1, pp. 1–7, 2017.

[13] H. R. Alemohammad, E. Foroozmehr, B. S. Cotten, and E. Toyserkani, "A dual-parameter optical fiber sensor for concurrent strain and temperature measurement : Design, fabrication, packaging, and calibration," *J. Lightw. Technol.*, vol. 31, no. 8, pp. 1198–1204, Apr. 2013.

[14] X. Fu, P. Lu, W. Ni, H. Liao, D. E. Liu, and J. Zhang, "Phase demodulation of interferometric fiber sensor based on fast Fourier analysis," *Opt. Exp.*, vol. 25, no. 18, pp. 1387–1390, 2017.

[15] L. Gounaridis *et al.*, "High performance refractive index sensor based on low Q-factor ring resonators and FFT processing of wavelength scanning data," *Opt. Exp.*, vol. 25, no. 7, 2017, Art. no. 7483.

[16] L. Gounaridis, P. Groumas, E. Schreuder, R. Heideman, H. Avramopoulos, and C. Kouloumentas, "New set of design rules for resonant refractive index sensors enabled by FFT based processing of the measurement data," *Opt. Exp.*, vol. 24, no. 7, pp. 7611–7632, 2016.

[17] Y. Jiang, "Fourier-transform phase comparator for the measurement of extrinsic Fabry-Perot interferometric sensors," *Microw. Opt. Technol. Lett.*, vol. 50, no. 10, pp. 2621–2625, 2008.

[18] J. Li *et al.*, "Ultrasensitive refractive index sensor based on enhanced Vernier effect through cascaded fiber core-offset pairs," *Opt. Exp.*, vol. 28, no. 3, 2020, Art. no. 4145.

[19] T. Nan *et al.*, "Optical fiber temperature sensor with insensitive refractive index and strain based on phase demodulation," *Microw. Opt. Technol. Lett.*, vol. 62, no. 12, pp. 3733–3738, 2020.

[20] M. Galarza, R. A. Perez-Herrera, D. Leandro, A. Judez, and M. López-Amo, "Spatial-frequency multiplexing of high-sensitivity liquid level sensors based on multimode interference micro-fibers," *Sensors Actuators, A: Phys.*, vol. 307, 2020, Art. no. 111985.

[21] C. Eigenwillig, B. Biedermann, and R. Huber, "Optical coherence tomography imaging with k-space linear Fourier domain mode locked lasers," *Opt. InfoBase Conf. Papers*, vol. 16, no. 12, pp. 2953–2963, 2008.

[22] T. Wu, Z. Ding, L. Wang, and M. Chen, "Spectral phase based k-domain interpolation for uniform sampling in swept-source optical coherence tomography," *Opt. Exp.*, vol. 19, no. 19, pp. 18430, 2011.

[23] Y. X. Xiao, J. Wang, Y. F. Hou, L. H. Zhang, and S. S. Wang, "Mode analysis of in-line Mach-Zehnder interferometer with offset splicing," *Opt. Fiber Technol.*, vol. 62, 2021, Art. no. 102473.

[24] T. Wei, X. Lan, and H. Xiao, "Fiber inline core-cladding-mode Mach-Zehnder interferometer fabricated by two-point CO_2 laser irradiations," *IEEE Photon. Technol. Lett.*, vol. 21, no. 10, pp. 669–671, May 2009.

[25] W. W. Li, D. N. Wang, Z. K. Wang, and B. Xu, "Fiber in-line Mach-Zehnder interferometer based on a pair of short sections of waveguide," *Opt. Exp.*, vol. 26, no. 9, pp. 11496–11502, 2018.

[26] C. Zhou, Q. Zhou, C. He, J. Tian, Y. Sun, and Y. Yao, "Fiber optic sensor for simultaneous measurement of refractive index and temperature based on internal-and-external-cavity Fabry-Pérot interferometer configuration," *IEEE Sensors J.*, vol. 21, no. 8, pp. 9877–9884, Apr. 2021.

[27] R. Oliveira, J. H. Osório, S. Aristilde, L. Bilro, R. N. Nogueira, and C. M. B. Cordeiro, "Simultaneous measurement of strain, temperature and refractive index based on multimode interference, fiber tapering and fiber Bragg gratings," *Meas. Sci. Technol.*, vol. 27, no. 7, 2016, Art. no. 075107.

[28] C. Gouveia, G. Chesini, C. M. B. Cordeiro, J. M. Baptista, and P. A. S. Jorge, "Simultaneous measurement of refractive index and temperature using multimode interference inside a high birefringence fiber loop mirror," *Sensors Actuators, B: Chem.*, vol. 177, pp. 717–723, 2013.

[29] T. Jiao *et al.*, "Simultaneous measurement of refractive index and temperature using a Mach-Zehnder interferometer with forward core-cladding-core recoupling," *Opt. Laser Technol.*, vol. 111, pp. 612–615, 2019.

[30] I. Pfalzgraf, S. Suntsov, and D. Kip, "Fiber-optic sensor measuring spatial distributions of refractive index and temperature," *Appl. Opt.*, vol. 60, no. 5, pp. 1428–1433, 2021.

[31] A. D. Gomes *et al.*, "Optical harmonic Vernier effect: A new tool for high performance interferometric fibre sensors," *Sensors*, vol. 19, no. 24, pp. 1–18, 2019.